Article

Design, Synthesis, and Evaluation of Novel Magnetic Nanoparticles Combined with Thiophene Derivatives for the Removal of Cr(VI) from an Aqueous Solution

Seham S. Alterary,* Monirah A. Al-Alshaikh, Athar M. Elhadi, and Wenjie Cao

Read Online

ACCESS | Metrics & More | Article Recommendations | SI Supporting Information

ABSTRACT: Most heavy metals are harmful to human health and the environment, even at extremely low concentrations. In natural waters, they are usually found only in trace amounts. Researchers are paying great attention to nanotechnology and nanomaterials as viable solutions to the problem of water pollution. This research focuses on the synthesis of organic thiophene derivatives that can be used as grafted ligands on the surface of silica-coated iron oxide nanoparticles to remove Cr(VI) chromium ions from water. The Vilsmeier−Haack reaction allows the formation of aldehyde groups in thiophene derivatives, and the resulting products were characterized by the FT-IR, NMR, and GC−MS. Schiff base is used as a binder between organic compounds and nanoparticles by the reaction of aldehyde groups in thiophene derivatives and amine groups on the surface of coated iron oxide nanoparticles. Schiff base functionalized Fe_3O_4 composites (MNPs@SiO$_2$-SB-THCA) and (MNPs@SiO$_2$-SB-THCTA) were successfully synthesized by homogeneous and heterogeneous methods and characterized by a combination of FT-IR, transmission electron microscopy, X-ray photoelectron spectroscopy, and thermogravimetric analysis. The adsorption studies, kinetic modeling, adsorption isotherms, and thermodynamics of the two materials, MNPs@SiO$_2$-SB-THCA and MNPs@SiO$_2$-SB-THCTA, were investigated for the removal of Cr(VI) from water at room temperature and at 50 mg/L. The high adsorption capacity at pH 6 for MNPs@SiO$_2$-SB-THCTA was 15.53 mg/g, and for MNPs@SiO$_2$-SB-THCA, it was 14.31 mg/g.

1. INTRODUCTION

A pure water source is necessary for a sustainable life. Water pollution is a major problem that threatens life on earth and damages the entire ecosystem. The alarming increase of hazardous pollutants in the aquatic environment is a result of industrial development, including the expansion of energy plants and the mining industry.[1]

Heavy metals can enter water bodies through a variety of industrial effluents, e.g., from the manufacture of metal and electronic equipment, mining, metal plating, and power generation plants.[2] Certain heavy metals found in water are highly toxic and nonbiodegradable. They can accumulate in low concentrations in living animals once they enter the food chain and have the potential to cause harmful effects such as damage to the nervous system, kidney failure, and cancer.[3]

Chromium (Cr), a naturally occurring heavy metal used in industry, is present in the earth's crust and the oceans. Cr species such as trivalent Cr(III) and hexavalent Cr(VI) are considered hazardous due to their high solubility and diffusivity, which allow them to easily penetrate biological membranes.[4] The use of nanomaterials in water treatment is very successful due to their large surface area, high potential surface reactivity, and absorption capacity.[5] Through the adsorption process on their surfaces, nanomaterials can be used to remove heavy metals from wastewater. It has been

proposed to remove heavy metal ions from aqueous solutions using magnetic nanomaterials. Magnetic nanoadsorbents have been found to be inexpensive, easy to use, environmentally friendly, and highly efficient in removing metals from large volumes of water and wastewater in a short time.[6] The magnetic properties of such nanoadsorbents could be used to separate adsorbents by applying an external magnetic field. Thus, nanoadsorbents that combine nanotechnology and magnetic separation techniques could be a successful technology for the remediation of heavy metal ions from water solutions.[7]

Khare et al. described the use of a new photocatalytic material (C−ZnO dots) for the photochemical degradation of Cr(VI) in dichromate water.[8] In a single microwave-assisted step, carbon dots encoded with nitrogen and sulfur were synthesized with a fluorescence quantum yield of 12% as a sunlight-active photomaterial for the removal of Cr(VI) from water.[9] Another study reports the use of nanocarbon as one of
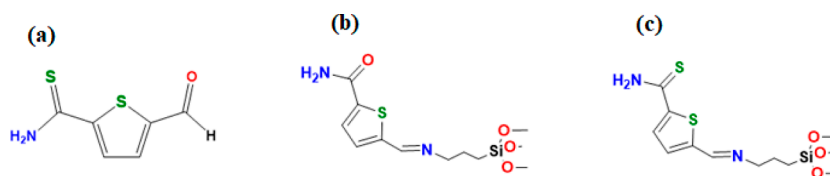
Scheme 1. Illustration of Novel Synthesized Compounds (a) 5-Formylthiophene-2-carbothioamide, (b) SB-THCA, and (c) SB-THCTA

the most promising nanomaterials for water filtration due to its surface reactivity, microporous shape, and specific structure.[10]

The comparatively high cost of carbon nanoparticles is a major obstacle to their use on an industrial scale for water filtration. Due to the associated health risks, the release of pollutant-laden, unrecovered carbon nanoparticles into the environment, and the resulting human exposure to carbon nanoparticles remain controversial.[11]

Magnetic nanoparticles are excellent candidates for wastewater treatment processes such as flocculation, demulsification, adsorption, filtration, and photocatalytic activities. The removal of impurities from solutions is efficient and easy when an external magnetic field is used.[12−15] The advantages of using iron oxide nanoparticles as adsorbents are environmental friendliness, easy separation from an aqueous solution by an external magnetic field, and fast interaction with impurities.[16] The physicochemical properties of the adsorbent for heavy metals and the operating conditions (temperature, adsorbent quantity, pH value, adsorption time, and initial concentration of the metal ions) determine the adsorption process. Heavy metal ions can be adsorbed on the surface of an adsorbent, and it is claimed that this technology has low operating costs, high removal capacity, easy implementation, and easy treatment by regeneration of the adsorbed heavy metal ions.[17] Magnetic adsorbents are material matrices containing iron particles (often magnetic nanoparticles, such as Fe_3O_4). The magnetic field, surface charge, and redox activity all affect the adsorption process. Several characteristics, such as the surface shape and magnetic behavior of the adsorbent, influence the mechanism and kinetics of the sorption process.[18]

The use of synthetically produced magnetite nanoparticles has become rare due to their low chemical resistance to strong acids and strong oxidizing agents. This disadvantage led to the loss of magnetic activity. Silicon dioxide has several advantages, such as good chemical resistance to organic solvents, easy functionalization, easy adhesion, and high binding strength to iron oxide.[19] Surface modification has the advantage of providing specific functional selectivity for ions, which increases the capacity of heavy metals in the water treatment method. Functionalized materials have been used by grafting chelating ligands onto the surface of nanomaterials.[20]

The surface of iron oxide nanoparticles has been functionalized with (−OH, −NH₂, −COOH, and −SH) so that they can be modified by attaching other molecules for a variety of purposes, such as applications that rely on thiophene derivatives, including those used as intermediates in coordination chemistry, organic synthesis, and materials science.[21,22] In addition, the sulfur group in thiophene is a soft Lewis base that provides some selectivity for binding to soft Lewis's acids.[23] Therefore, improved sulfur coordination and binding affinity have been developed for thiophene, along with additional electron donor groups.[24]

Heterocyclic Schiff bases have unique chelating properties due to the presence of S, O, and N donor atoms.[25] Schiff bases have gained acceptance in coordination chemistry because they can form a stable complex with a transition metal, and mesoporous silica materials immobilized with Schiff bases offer great potential for the removal of heavy metal ions.[26] In general, a Schiff base is a compound with an azomethine functional group (−HC=N) formed by primary amines with aldehyde or ketone.[27]

The depletion of freshwater supplies caused by heavy metal pollution is a serious global problem, with severe consequences for environmental protection and human health. Therefore, it is crucial to use novel methods to develop and synthesize ecological, efficient, and cost-effective materials for the detection and removal of heavy metal ions. This research focuses on the development of a novel material using magnetic nanoparticles and thiophene derivatives. The newly synthesized magnetic nanoparticles in combination with thiophene derivatives were used to investigate their adsorption capacities for the removal of Cr(VI) ions from an aqueous medium. The removal of Cr(VI) from contaminated water was carried out by investigating and optimizing various experimental conditions, including the initial concentration of Cr(IV), contact time, pH, and sorbent dose, as well as studying the adsorption kinetics, isothermal modeling, and thermodynamic mechanisms.

2. EXPERIMENTAL SECTION

2.1. Materials. Pure chemicals, including 3-aminopropyl-triethoxysilane (APTES, 99%), tetraethoxysilane (TEOS, 98%), and 2-thiophene carboxamide (99%), were purchased from Sigma-Aldrich, Hamburg, Germany. Ferric chloride hexahydrate (99%) and phosphorus oxychloride (POCl₃, 99%) were supplied by (Loba Chemie Pvt. Ltd., Mumbai, India). Ethylene glycol (99.8%) and trisodium citrate dehydrate (99.2%) were supplied by (BDH Ltd., Pool, United Kingdom). In addition, sodium acetate anhydrous (99%) was supplied by (ROMIL Pure Chemistry, Cambridge, United Kingdom) and N,N-dimethylformamide (DMF, 99.99%) by Fisher Scientific, PA, USA. Other chemicals such as trisodium citrate dehydrate (99.2%) and thiophene-2-thiocarboxamide were purchased from Atlantic Research Group, Charlottesville, USA.

2.2. Preparation of Organic Compounds. The Vilsmeier−Haack reaction was carried out by slowly adding 2.0 mL of phosphorus oxychloride (POCl₃) to 3.0 mL of ice-cooled DMF, with constant stirring for 30 min. Then, the starting materials were added to the formed mixture with constant stirring for 48 h at room temperature. The resulting solution was neutralized with a saturated sodium acetate solution. For thiophene carboxamide, the aqueous layer was generally extracted 3 times with 15 mL of ethyl acetate (3 × 15 mL). For thiophene carbothioamide, the aqueous layer was extracted with dichloromethane (3 × 15 mL), and the organic

fraction was then dried with anhydrous magnesium sulfate. Scheme 1 shows the novel part of the synthesized nanomaterials.

2.3. Characterization and Yield of the Synthesized Organic Compounds.
The prepared 5-formylthiophene-2-carboxamide showed:

Amount and appearance: 0.46 g (57%) as a white solid and melting point (155 °C).

IR: ν_{max}/cm^{-1}: 3452, 3216, 3158, 3096, 2942, 1720, 1668, 1524, 1474, 826, 790, 732.

NMR: δH 10.18 (s, 1H), 9.34 (d, J = 9.6 Hz, 1H), 7.94 (d, J = 3.9 Hz, 1H), 7.73 (d, J = 5.0 Hz, 1H), 7.20 (t, J = 4.5 Hz, 1H). δC 164.6, 161, 136.1, 134.8, 131.9, 128.7.

GC−MS: for 5-formylthiophene-2-carboxamide, the retention time was at around 8 min, and the exact mass was 155 m/z, M + 1 = 156 m/z, and M + 2 = 157 m/z.

The prepared 5-formylthiophene-2-carbothioamide showed:

Amount and appearance: 0.36 g (62%) orange solid produced and melting point (145 °C).

IR: ν_{max}/cm^{-1}: 3428, 3218, 3160, 3098, 2924, 2856, 1722, 1672, 1524, 1478, 826, 790, 736.

NMR: δH 10.32 (s, 1H), 9.34 (d, J = 9.3 Hz, 1H), 8.03−7.93 (m, 1H), 7.72 (dd, J = 5.0, 1.3 Hz, 1H), 7.19 (td, J = 4.3, 1.1 Hz, 1H). δC 164.7, 161.1, 136.2, 134.8, 131.9, 128.7.

GC−MS: for 5-formylthiophene-2-carbothioamide, the retention time was 4.540 min, and the exact mass was 171 m/z and M + 2 = 173 m/z.

2.4. Synthesis of Magnetite Nanoparticles (Fe$_3$O$_4$).
Magnetite nanoparticles (Fe$_3$O$_4$) were synthesized by mixing FeCl$_3$·6H$_2$O (0.67 g, 2.5 mmol), anhydrous sodium acetate (1.80 g, 22 mmol), trisodium citrate dihydrate (0.2 g, 0.68 mmol), and ethylene glycol (20 mL) with vigorous stirring until a homogeneous deep yellow solution was obtained. To complete the reaction, 50 mL of the resulting solution was autoclaved at 185 °C for 8 h. The resulting product was cooled to room temperature and separated magnetically. The separated product was washed several times with ethanol and then with acetone and dried in an oven at 70 °C for 6 h. The product was then removed from the solution.

2.5. Synthesis of Modified Silica-Coated Magnetic Nanoparticles.
Modified silica-coated magnetic nanoparticles (Fe$_3$O$_4$@SiO$_2$−NH$_2$) were synthesized by suspending 50 mg of the prepared Fe$_3$O$_4$ nanoparticles in a mixture of 10 mL of deionized water, 40 mL of ethanol, and 500 μL of ammonia solution under ultrasonic treatment for 30 min. Then, 30 μL of TEOS was added dropwise to the above solution and stored at room temperature for 6 h. About 300 μL of APTES was added dropwise to the above solution, and the reaction was continued for 24 h. The resulting product was magnetically separated, washed several times with ethanol, and then dried in an oven at 60 °C for 6 h.[28]

2.6. Grafting of Organic Compound.
2.6.1. Heterogeneous Technique. MNPs@SiO$_2$-SB-THCA was synthesized by adding 0.06 g of Fe$_3$O$_4$@SiO$_2$−NH$_2$ suspended in 10 mL of methanol to a solution of 5-formyl-2-thiophene carboxamide (0.08 g, 0.49 mmol) suspended in 10 mL of methanol, followed by a few drops of acetic acid. After refluxing for 3 h, the resulting product was magnetically separated, washed several times with methanol, and then dried in an oven at 60 °C for 6 h.[29] Accordingly, the synthesis of MNPs@SiO$_2$-SB-THCTA with 5-formylthiophene-2-carbothioamide (0.08 g, 0.44 mmol) was done according to the procedure described above.

*2.6.2. Homogeneous Technique.* MNPs@SiO$_2$-SB-THCA was synthesized by mixing 5-formylthiophene-2-carboxamide (0.14 g, 0.94 mmol) dissolved in 12 mL of tetrahydrofuran with 0.1 mL of (3-aminopropyl)-triethoxysilane under magnetic stirring for 48 h at room temperature to produce SB-THCA. The excess solvent was removed by filtration to obtain a white precipitate. The resulting precipitate was dried in an oven at 50 °C for 1 h. In addition, 0.06 g of SiO$_2$-MNPs and 0.14 g of SB-thiophene-2-carboxamide were dispersed in 40 mL of ethanol. The dispersed mixture was then heated at 76 °C under a nitrogen atmosphere for 24 h with constant stirring.

The resulting material was separated magnetically, washed several times with hot ethanol, and then dried in an oven at 60 °C for 6 h. MNPs@SiO$_2$-SB-THCTA was synthesized by mixing 5-formylthiophene-2-carbothioamide (0.14 g, 0.85 mmol), 0.1 mL of (3-aminopropyl)-triethoxysilane, and 12 mL of tetrahydrofuran under magnetic stirring at room temperature for 48 h. The resulting material was then separated by magnetic stirring. The resulting material was then separated by magnetic separation. Subsequently, 0.06 g of SiO$_2$-MNPs and 0.14 g of SB-thiophene-2-carbothioamide were dispersed in 40 mL of ethanol. The suspension was then stirred at 76 °C for 2 h, followed by constant stirring for 24 h under a nitrogen atmosphere. The resulting MNPs@SiO$_2$-SB-THCTA was recovered after magnetic separation, washed several times with hot ethanol, and then oven-dried at 60 °C for 6 h.

2.7. Characterizations.
The ^{1}H and ^{13}C NMR spectra were recorded using the JEOL RESONCE 500 (Tokyo, Japan) and the solvent peak reference: CDCl$_3$ δ = 7.26 (^{1}H) and δ = 77.0 (^{13}C) ppm. The chemical shifts of δ are given in ppm. Fourier transform infrared (FT-IR) spectra were measured using a PerkinElmer Spectrum BX (Waltham, USA) at wavenumbers in the range of 4400−400 cm^{-1}. The X-ray diffraction (XRD) pattern was used to study the crystallite shape and size of the formed Fe$_3$O$_4$ and Fe$_3$O$_4$@SiO$_2$ nanomaterials. Mass spectra were obtained using an Agilent GC−MS instrument (Agilent, Santa Clara, California, USA). Transmission electron microscopy (TEM) images were obtained using a JEOL JEM-1400 TEM (Tokyo, Japan) at 100 kV. An X-ray photoelectron spectroscopy (XPS) measurement was used to confirm the surface modification of the organic compounds by heterogeneous and homogeneous methods. Thermogravimetric analysis (TGA) was performed on a PerkinElmer Pyris 1 TGA instrument (PerkinElmer, Waltham, USA) with a heating rate of 10 °C/min and a temperature range of 25−700 °C under a nitrogen atmosphere. Inductively coupled plasma mass spectrometry (ICP−MS, Tucson, USA) was used to determine the Cr(VI) concentration before and after adsorption. All samples were diluted to 1 ppm for measurement with the Thermo Scientific iCAPQ ICP MS. The pH of each solution was adjusted with a SevenCompact pH meter S220 by adding HCl or KOH.

2.8. Adsorption Studies.
Batch experiments were performed to study the Cr(VI) adsorption on MNPs@SiO$_2$-SB-THCA and MNPs@SiO$_2$-SB-THCTA at room temperature (25 °C). Approximately 10 mL of Cr(VI) solution with different initial concentrations (10 to 50 mg/L) were shaken at 350 rpm using a (Remi CIS4BL orbital shaker) with a predefined dosage of 10 mg adsorbent. Samples were filtered using Whatman filter paper no. 42, and the filtrate was analyzed for residual Cr(VI) content using a spectropho-
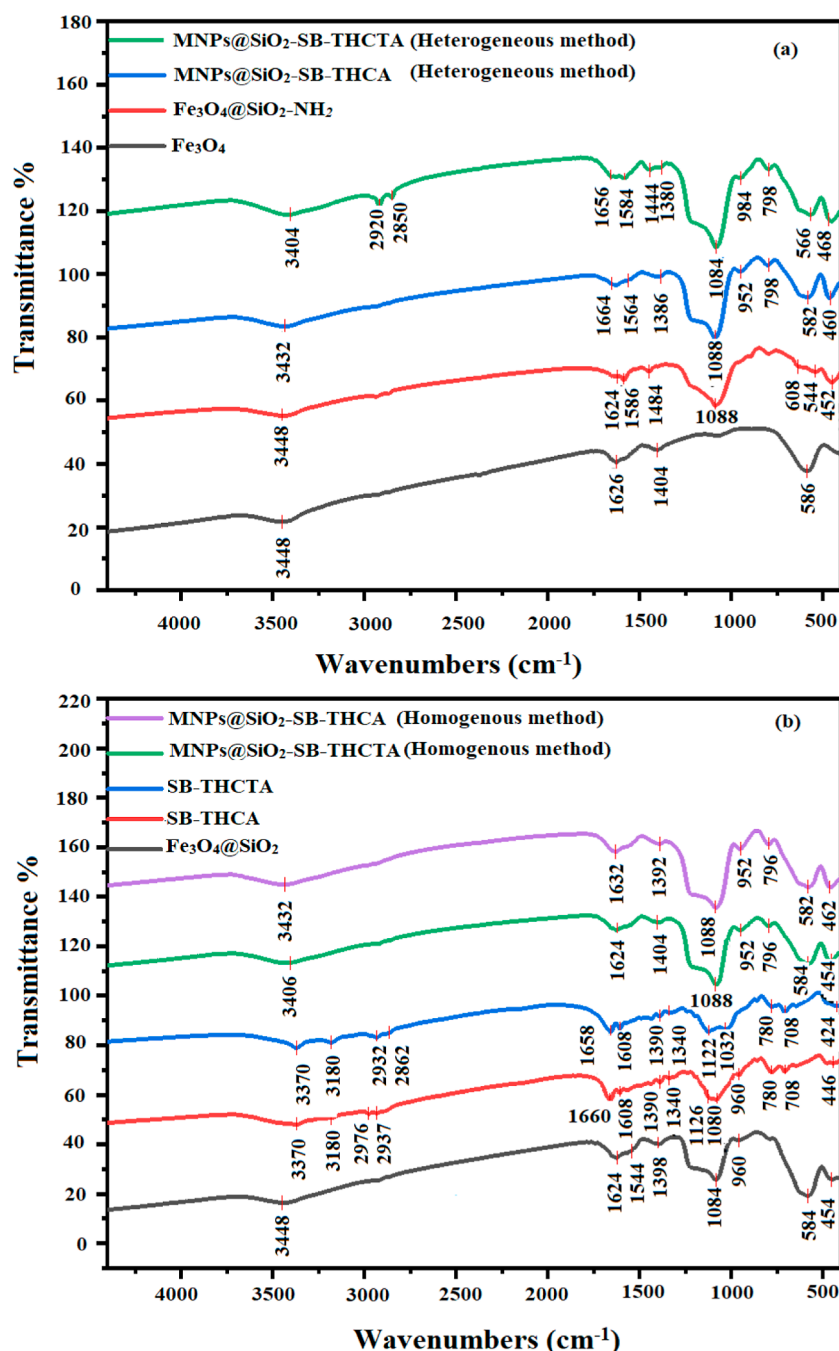
Figure 1. FT-IR spectra of (a) Fe_3O_4, $Fe_3O_4@SiO_2-NH_2$, MNPs@SiO_2-SB-THCA, and MNPs@SiO_2-SB-THCTA (heterogeneous method) and (b) $Fe_3O_4@SiO_2$, SB-THCA, SB-THCTA, MNPs@SiO_2-SB-THCA, and MNPs@SiO_2-SB-THCTA (homogeneous method).

tometer (Shimadzu, Kyoto, Japan) at 543 nm in the presence of diphenyl carbazide. The calibrations were performed with Cr(VI) standard solutions with concentrations of 10−250 mg/L. To improve the reading accuracy, a 1:1 ratio of the buffer solution was used to adjust the total ionic strength with the sample solutions for detection to eliminate any interference in the analyte solution. The amount of adsorbed Cr(IV) was calculated using eq 1

$$q_e = \frac{C_0 - C_e}{M} \times V \tag{1}$$

The values q_e, C_0, and C_e indicate the equilibrium concentration of Cr(VI) ions in mg/g, C_e represents the initial

concentration of Cr(VI), V and M indicate the volume of the solution in L and the dose of adsorbent in g/L. All batch experiments were repeated, and in the results and discussions, the mean of the values was used as the error bar, serving as the standard deviation.

3. RESULTS AND DISCUSSION

3.1. Characterization. The characterization of thiophene carboxamide and thiophene carbothioamide was performed using various spectroscopic and microscopic techniques including FT-IR, XRD, NMR, TGA, TEM, and XPS.

3.1.1. FT-IR Analysis. The adsorption peaks in the range 1720−1728 cm^{-1} were assigned to the aldehyde groups. The
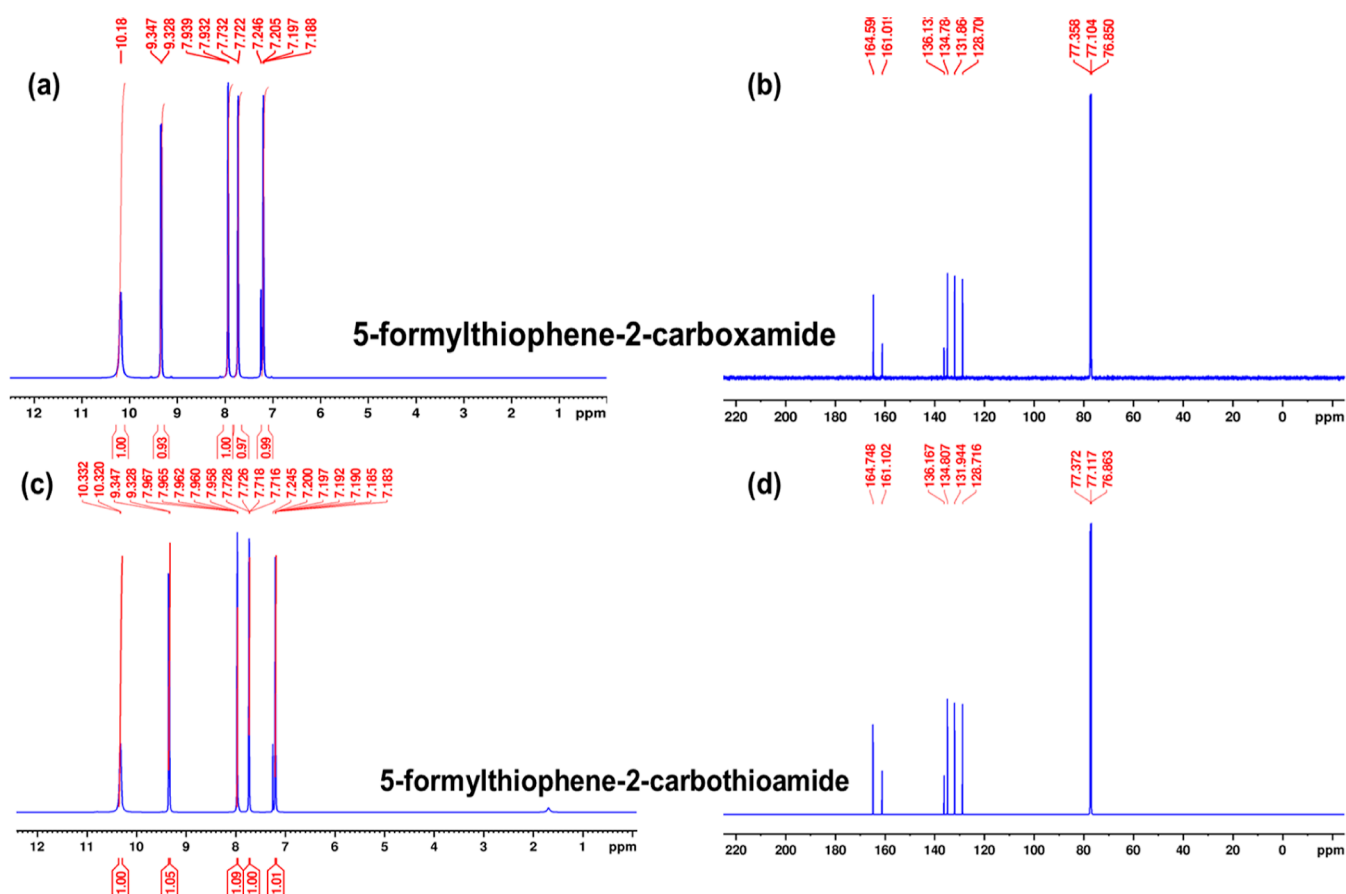
Figure 2. (a,b) and (c,d) ^{1}H NMR and ^{13}C NMR spectra of 5-formylthiophene-2-carboxamide and 5-formylthiophene-2-carbothioamide, respectively.

two peaks observed at 2924−2858 cm^{-1} correspond to the (C−H) stretching mode of the hydrogen aldehyde. However, the stretching peaks at 1674 and 1668 cm^{-1} were assigned to the carbonyl groups of the amides. The two significant peaks at 3216−3176 cm^{-1} corresponded to the (N−H) stretching vibrations of the primary amides. The occurring C═S stretching vibration band can be detected at 1672 and 1670 cm^{-1}.[30] The FT-IR spectra of Fe$_3$O$_4$, Fe$_3$O$_4$@SiO$_2$, and Fe$_3$O$_4$@SiO$_2$−NH$_2$ samples were characterized according to a previously published study.[31] The peaks of the stretching vibrations appeared at 3448 and 3434 cm^{-1} and represented the O−H group. The Fe−O showed a vibrational peak at 586 cm^{-1} in the Fe$_3$O$_4$ and Fe$_3$O$_4$@SiO$_2$ samples. The strong absorption peaks that appeared at 1088 cm^{-1} were due to Si− O−Si stretching vibrations in the Fe$_3$O$_4$@SiO$_2$ and Fe$_3$O$_4$@ SiO$_2$−NH$_2$ samples. New absorption peaks appeared at 2938 and 2872 cm^{-1} for the Fe$_3$O$_4$@SiO$_2$−NH$_2$ sample, which belong to asymmetric and symmetric absorption CH$_2$. This indicates that the aminopropyl groups were successfully introduced onto the surface of Fe$_3$O$_4$@SiO$_2$.

The FT-IR spectra of the Schiff base synthesized by the reaction of APTS and organic compounds showed that the peak at 1658 cm^{-1} corresponded to C═S stretching and that at 1660 cm^{-1} corresponded to C═O stretching. The new absorption peaks at 1610 and 1608 cm^{-1} belong to the C═N stretching vibration, as found in a previous study.[32]

Two techniques (homogeneous and heterogeneous) were used to prepare synthetic nanoparticles grafted with organic ligands, as shown in the FT-IR spectra. The peaks in the

spectra attributed to the Si−O−Si stretching vibration are found at 1084 and 1088 cm^{-1}. C═N bonds are indicated by the absorption peaks at 1626 cm^{-1}. The NH$_2$ mode is responsible for the absorption peak of MNPs-SiO$_2$-SB-THCTA (heterogeneous method) at 1584 cm^{-1}. According to the symmetric and asymmetric stretching of the CH$_2$ band in aminopropyl groups, the two absorption maxima were recorded at 2920 and 2850 cm^{-1}. This indicates that some NH$_2$ groups did not interact with the organic molecules in the heterogeneous approach of MNPs-SiO$_2$-SB-THCTA. Absorption peaks at 1397 and 1386 cm^{-1} were detected in both the homogeneous and heterogeneous methods, which are related to the C−N stretching of the primary amide (Figure 1a,b).

3.1.2. NMR Detection. ^{1}H NMR was used to confirm the structures of thiophene carboxamide and thiophene carbothioamide. These compounds showed a broad singlet peak at δ = 10.18 and 10.32 ppm due to the proton of the aldehyde. The N−H proton appeared in two different peaks due to the nonequivalence of the amide proton, which was apparently prevented from rotating, and this rapid rotation was detected by NMR.[33]

The N−H proton peak appears at δ = 9.34 and 7.72 ppm of the doublet signal. The C−H proton for thiophene appears at 8.03−7.93 ppm (multiplet signal) and 7.42 ppm (triplet of doublet signal), as shown in Figure 2c. The ^{13}C NMR spectra: the carbonyl group of the amide appears at δC 164.7 ppm and the C═O group of the aldehyde at 161.1 ppm. The other peaks appeared at 136.2, 134.8, 131.9, and 128.7 ppm, as

shown in Figure 2d. These results confirmed the structure of the 5-formylthiophene-2-carbothioamide compound.

3.1.3. XRD Analysis. The XRD diagram of magnetite Fe_3O_4NPs (Figure 3) shows the presence of different
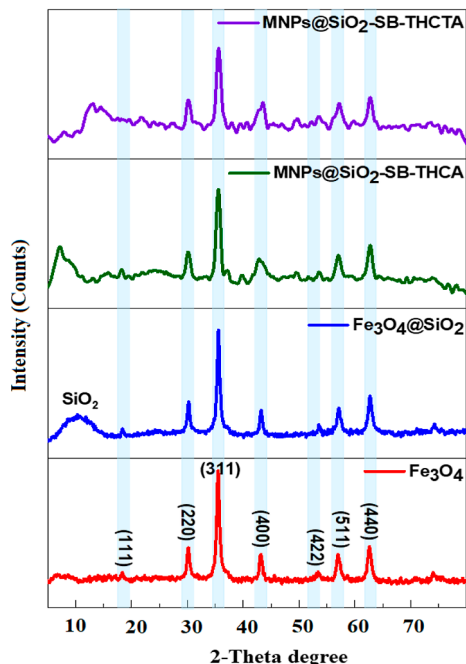
Figure 3. XRD spectra of Fe_3O_4, $Fe_3O_4@SiO_2$, MNPs@SiO$_2$-THCA, and MNPs@SiO$_2$-SB-THCTA.

diffraction peaks at 2θ values of 18, 30, 45.4, 43, 53.4, 56.9, and 62.5°, which can be assigned to crystalline planes (111), (220), (311), (400), (422), (511), and (440), respectively. These results indicate the formation of cubic magnetite phases consistent with JCPDS map no. 01-075-0449.[34] The size of the crystalline particles was calculated using Scherrer (eq 2), using the peak at 35.7° (311)

$$D = 0.9\lambda/\beta \cos \theta \qquad (2)$$

D, λ, and β stand for the size of the crystallite particles, the X-ray wavelength (0.154 nm), the full width at half-maximum (fwhm), and the diffraction angle, respectively. The results show that the calculated crystallite size is 18.0 nm. Meanwhile, the XRD pattern of $Fe_3O_4@SiO_2$ (Figure 3) showed almost the same peaks, with a broad peak of SiO_2 at $2\theta = 23°$.[35] After the functionalization of Fe_3O_4 with organic compounds, the position of the characteristic Fe_3O_4 peaks in the XRD pattern remained unchanged. However, there were differences in the amorphous peaks in the 2θ range 10−15, which were attributed to the presence of silica and organic compounds (Figure 3).

3.1.4. TEM Detection. The TEM images with the particle size distributions were created using ImageJ software. The size distribution of Fe_3O_4 was estimated to be approximately 126.36 nm and $Fe_3O_4@SiO_2$ approximately 132.54 nm. The size distribution of $Fe_3O_4@SiO_2$−NH$_2$ was approximately 156.7 nm. As shown in Figure 4A−D, the size distribution for the heterogeneous method samples was approximately 156.1 nm for MNPs@SiO$_2$-SB-THCA (A) and approximately 140.15 nm for MNPs@SiO$_2$-SB-THCTA (B). The homogeneous method was approximately 139.38 nm for MNPs@SiO$_2$-SB-THCA (C), and the other size distribution was approximately 139.19 nm related to MNPs@SiO$_2$-SB-THCTA (D).

3.1.5. XPS Analysis. XPS analysis was also used to investigate the chemical elements present on the surface of MNPs@SiO$_2$-SB-THCA and MNPs@SiO$_2$-SB-THCTA. The element composition is summarized in Table 1. The C 1s and N 1s binding energy of MNPs@SiO$_2$-SB-THCA and MNPs@SiO$_2$-SB-THCTA samples prepared by heterogeneous and homogeneous methods was studied (Figure 5). At the C 1s region, five peaks have been properly fitted with binding energies of 286.2, 286.3, 286.6, and 286.6 eV for the C=N bond. The spectra showed the appearance of C−C at 287.2, 287.7, 286.9, and 287.44 eV. The binding energy at 284.9, 284.5, 284.7, and 283.5 eV expressed the presence of C−S/C−H. The spectra also showed the appearance of C=C at 288.6, 288.1, and 288 eV. The binding energy of −C=O−NH/−C=S−NH was found to be 289.9, 289.6, 289.5, and 289.2 eV (Figure 5a−d). The binding energies of the C=N bond have been reported in the literature.[36]
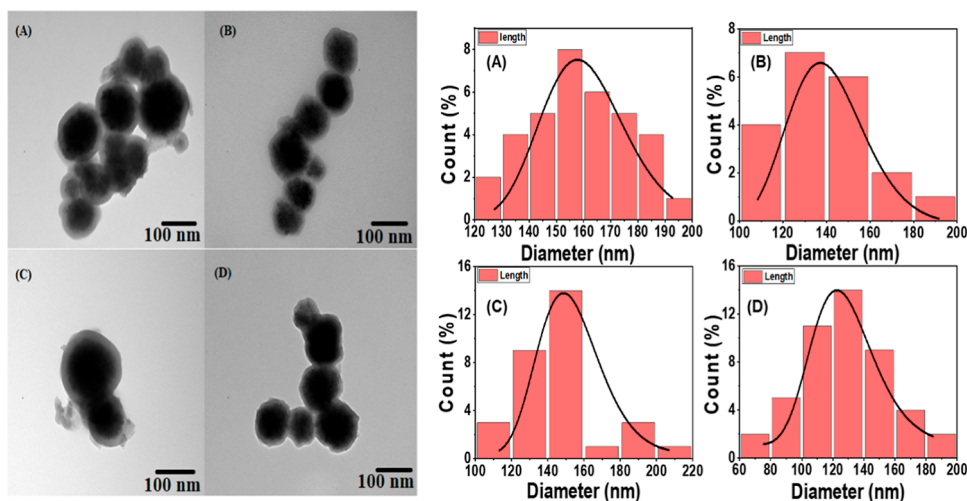
Figure 4. TEM images with size distribution of (A) MNPs@SiO$_2$-SB-THCA (heterogeneous method), (B) MNPs@SiO$_2$-SB-THCA (homogeneous method), (C) MNPs@SiO$_2$-SB-THCTA (heterogeneous method), and (D) MNPs@SiO$_2$-SB-THCTA (homogeneous method).

Table 1. Atomic Percentage of Element Measured by XPS

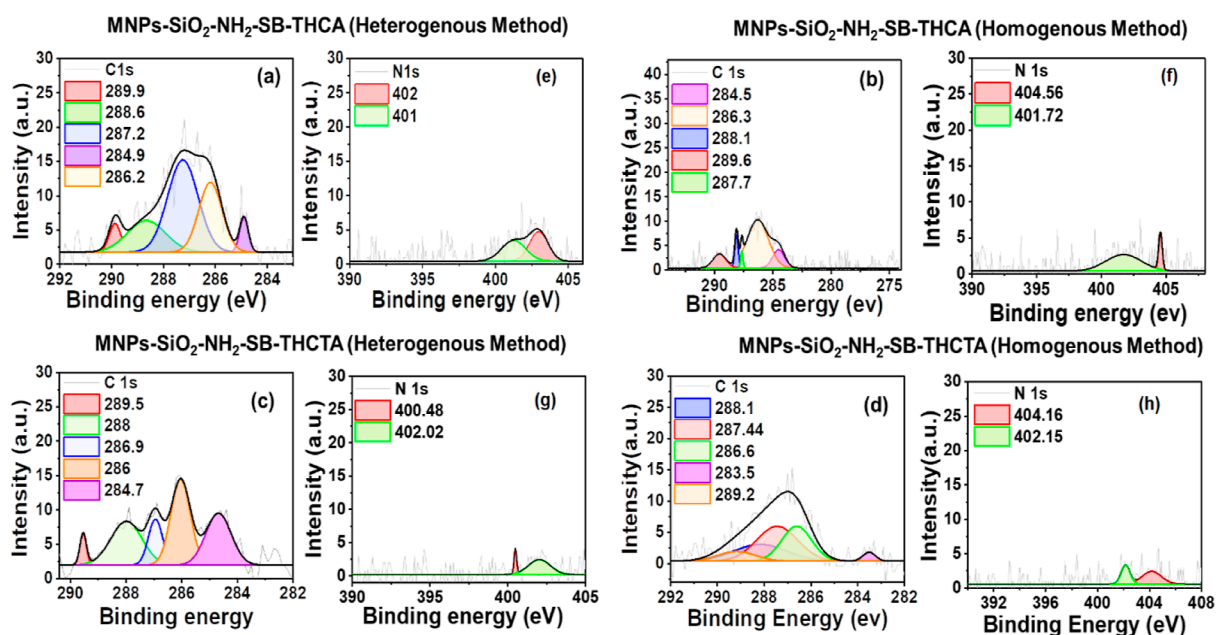| sample	BE/eV				atomic/%					
	C 1s		N 1s		C 1s	N 1s	Si 2p	S 2p	O 1s	Fe 2p
MNPs-SiO$_2$-NH$_2$-SB THCA (heterogeneous method)	C=N	286.2	C=N	401	15.02	2.31	22.29	17.23	43.24	5.17
	C−C	287.2	−C=O−NH$_2$	402						
	C−S/C−H	284.9								
	C=C	288.6								
	−C=O−NH$_2$	289.9								
MNPs-SiO$_2$-NH$_2$-SB-THCA (homogeneous method)	C=N	286.3	C=N	401.7	18.32	3.49	14.71	9.65	53.83	2.11
	C−C	287.7	−C=S−NH$_2$	404.56						
	C−S/C−H	284.5								
	C=C	288.1								
	−C=S−NH$_2$	289.6								
MNPs-SiO$_2$-NH$_2$-SB-THCTA (heterogeneous method)	C=N	286.6	C=N	400.48	22.29	2.74	15.78	4.87	54.32	5.72
	C−C	286.9	−C=O−NH$_2$	402.02						
	C−S/C−H	284.7								
	C=C	288								
	−C=O−NH$_2$	289.5								
MNPs-SiO$_2$-NH$_2$-SB-THCTA (homogeneous method)	C=N	286.6	C=N	402.15	9.44	1.92	26.61	11.68	50.35	0.53
	C−C	287.44	−C=S−NH$_2$	404.16						
	C−S/C−H	283.5								
	C=C	288.1								
	−C=S−NH$_2$	289.2								

Figure 5. XPS spectra of (a−d) MNPs@SiO$_2$-SB-THCA (heterogeneous and homogeneous methods) and (e−h) MNPs@SiO$_2$-SB-THCTA (heterogeneous and homogeneous methods).

In the N 1s region, two peaks have been properly fitted with binding energies of 401, 401.7, 400, and 402 eV representing the imine group. The binding energies 402 and 404 represent amide. In the heterogeneous method, a Fe 2p atomic percentage is greater than that of the homogeneous method. This showed that the homogeneous technique displayed excellent efficiency to cover the nanoparticle surfaces. The N 1s atomic percentage for nitrogen in the substance MNPs-SiO$_2$-SB-THCTA was higher than that of other methods, indicating that some unbonded NH$_2$ was present at the surface (Figure 5e−h).

3.1.6. TGA Analysis. The thermogram of MNPs@SiO$_2$-SB-THCA prepared by the heterogeneous method showed the first weight loss (3.12%) in the temperature range (25−138 °C) and, for the homogeneous method, the temperature range (25−200 °C) was about (5%). In the MNPs@SiO$_2$-SB-THCTA thermogram, the weight loss was about (3.3%) in the temperature range (25−170 °C) and about (3.06%) for the homogeneous method in the temperature range (25−144 °C).

The total weight loss in the first step is due to the removal of water molecules and the solvent used in the preparation (Figure 6).
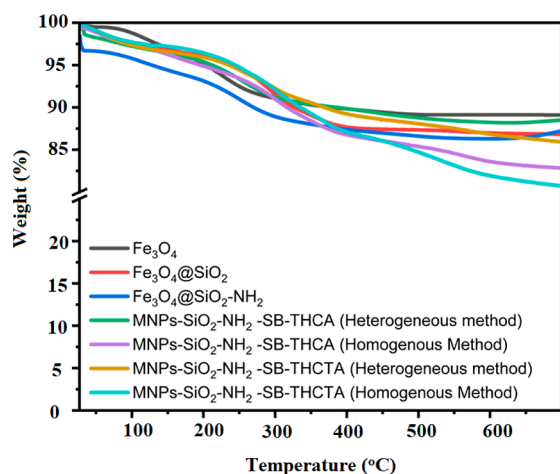
Figure 6. TGA graph of the MNPs@SiO$_2$-SB-THCA and MNPs@ SiO$_2$-SB-THCTA in the temperature range from 25 to 700 °C.

The second area was due to the decomposition of the Schiff base, as shown in Table 2. The results in the table show that

Table 2. Loss of Weight in the Decomposition of Schiff Base

samples		temperature (°C)	loss of weight (%)
MNPs-SiO$_2$-SB-THCA	heterogeneous method	138–295	8.9
	homogeneous method	200–384	12.8
MNPs-SiO$_2$-SB-THCTA	heterogeneous method	170–387	10.8
	homogeneous method	144–387	12.57

grafting by the homogeneous method has more weight loss than the heterogeneous method. The remaining weight loss is due to the condensation of the remaining silanol groups, as found in a previous study.[37]

As shown in Table 2, the temperature ranges of weight loss in the decomposition of Schiff bases are different, which is due to the different composition of the two methods (homogeneous and heterogeneous), as shown in the XPS table and confirmed by EDX and mapping analysis.

3.1.7. EDX Analysis. The EDX analysis for SB-THCA and SB-THCTA was used to indicate the amount of element for the intermediate compounds for the homogeneous method. The presence of silica, sulfur, and nitrogen indicates the successful interaction between the amine and aldehyde to form Schiff base (Figure 7a,b). Element mapping showed the differences in element distribution.

3.2. Factors Affecting Removal of Cr(VI). *3.2.1. Effect of Initial Concentration of Cr(VI).* To study the effect of initial Cr(VI) concentration on adsorption quantity, 50 mg/L MNPs@SiO$_2$-SB-THCA and MNPs@SiO$_2$-SB-THCTA were dispersed independently for 3 h in 10−50 mg/L Cr(VI) solution. According to the reports, the adsorption rate is quick initially and subsequently slows down as the Cr(VI) content increases (Figure 8a). The competition for active adsorption

sites grows as the Cr(VI) level increases, and the adsorption process slows.[38]

3.2.2. Effect of Contact Time. Contact time is an important parameter because it affects sorbate kinetics at a given initial concentration.[39] Using an equilibrium dose of MNPs@SiO$_2$-SB-THCA and MNPs@SiO$_2$-SB-THCTA, the effect of contact time was studied by varying the time duration from 0 to 120 min. Figure 8b shows the rapid adsorption of Cr(VI) ions in 60 min. After that, the process slows down and approaches equilibrium after 120 min. The adsorption did not increase significantly (less than 1%) when the contact time was extended up to 6 h, suggesting that adsorption could be completed in 2 h.

3.2.3. Effect of Amount of Adsorbent. The effect of presynthesized adsorbents MNPs-SiO$_2$-SB-THCA and MNPs-SiO$_2$-SB-THCTA dosages on the adsorption of Cr(VI) ions was investigated using different adsorbent dosages in the range of 10−80 mg/L. The percent removal of Cr(VI) ions increases significantly with the adsorbent dosage, which is attributed to increasing the adsorbent dosage increasing the number of active sites.[40] Adsorption was found to be uniform at adsorbent dosages greater than 50 mg/L. Therefore, in all subsequent experiments, an adsorbent dosage of 10 mg/L was determined to be the optimum dose for relatively acceptable Cr(VI) ion removal efficiency (Figure 8c).

3.2.4. Effect of Initial pH Values and Sorption Mechanism. In the case of functionality, the surface has organic molecules that interact with metal ions through electrostatic interaction, complex formation, or even hydrogen bonding. The pH value of the initial solution is an important factor influencing the adsorption of heavy metal ions. It affects both the surface charge of the adsorbents and the type of metal ions present in the solution. Higher pH values, for example, were not investigated due to the precipitation of metal ions. As shown in Figure 8d, pH 6 increases the removal of Cr(VI). This result can be explained by the protonation effect in the presence of N and S atoms of the Schiff bases.

At a low pH value of the solution, the high concentration of H$^+$ ions in the adsorbent competes with heavy metal ions for active binding sites. At a higher pH value, the surface of the adsorbent has a greater negative charge, which leads to an increased attraction of cations. The pH value of the sample is one of the most important factors in the adsorption process, as it influences the specification of the adsorbate, the degree of ionization, and the surface charge of the adsorbent (Figure 9).

The influence of pH on Cr(VI) remediation using MNPs-SiO$_2$-SB-THCA and MNPs-SiO$_2$-SB-THCTA was studied in the pH range of 2−8. The pH value of the samples was changed with 0.1 mol L^{-1} potassium hydroxide or hydrochloric acid. The percentage removal of Cr(VI) ions was plotted against the initial change in pH. The results showed that the adsorption of Cr(VI) ions on the surface of the adsorbents is pH-sensitive. For environmental studies, a pH of 8.4 was used for all experimental determinations, as the WHO/USEPA/BIS standards specify that the pH of drinking water should be in the range of 6.23 to 8.17.[41]

The adsorbent efficiency of MNPs-SiO$_2$-SB-THCA and MNPs-SiO$_2$-SB-THCTA was tested at different pH values ranging from 2 to 8 with other experimental conditions constant (agitation rate: 350 rpm, adsorbent dosage 10 mg/L, room temperature, contact time 2 h). The findings show that at acidic pH (2−6), the percentage of Cr(VI) removal was found to be greater than 51.9 and 74.47%, for MNPs-SiO$_2$-SB-
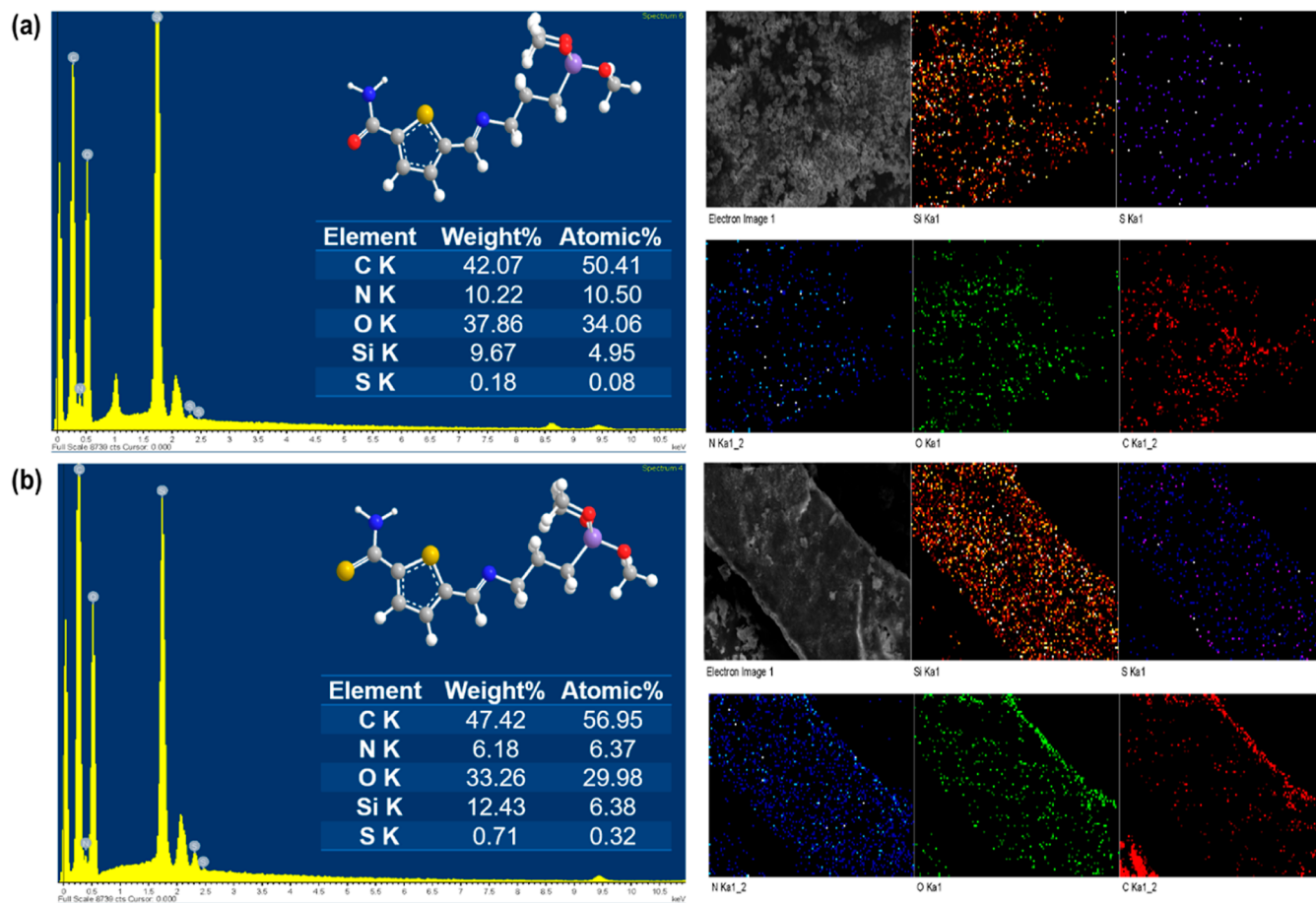
Figure 7. EDX spectra, mapping images of all elements, and atomic percentages of (a) SB-THCA and (b) SB-THCTA.
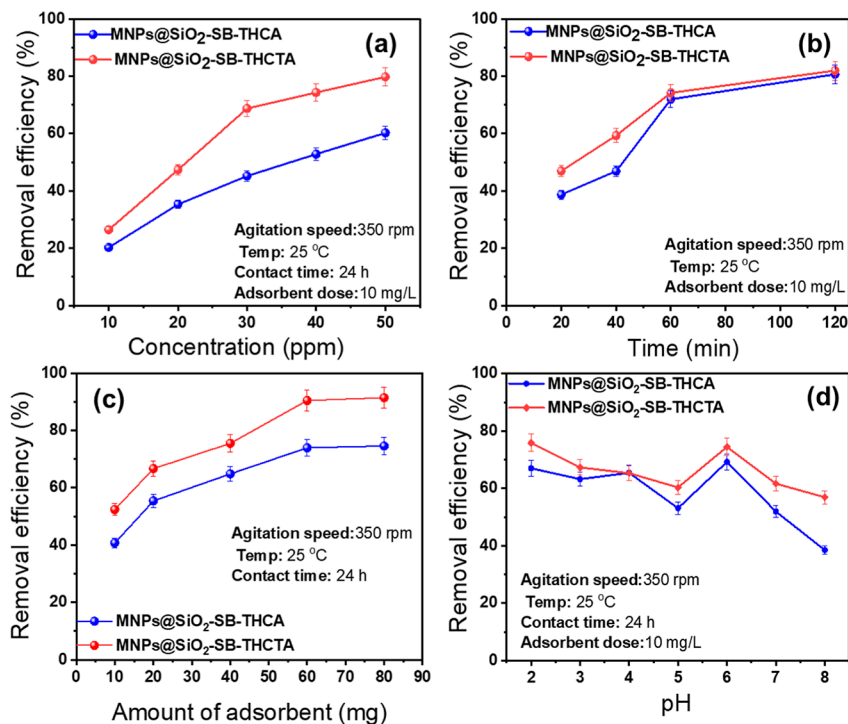

Figure 8. Optimization parameters for adsorption of Cr(VI) on the surface of MNPs-SiO$_2$-SB-THCA and MNPs-SiO$_2$-SB-THCTA (a) effect of the initial concentration of Cr(VI) solution, (b) effect of contact time (min), (c) effect of adsorption dosage (mg/L), and (d) effect of the initial pH of Cr(VI) solution in the range of 2−8.
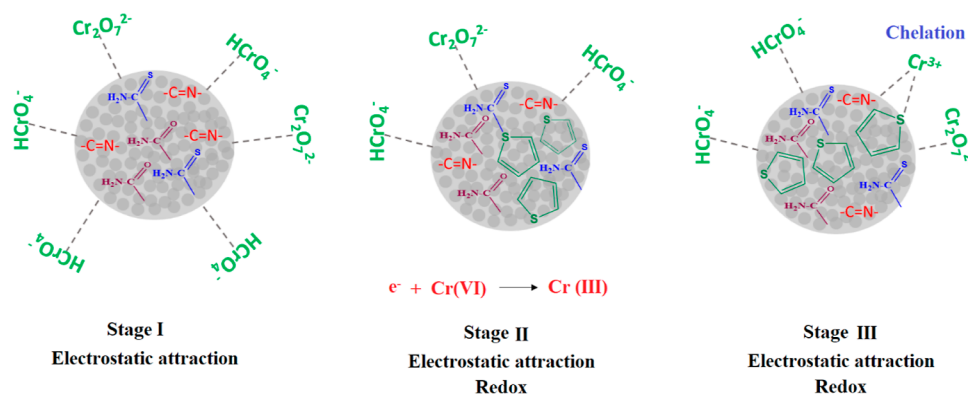
Figure 9. Possible mechanism of Cr(VI) removal using MNPs@SiO$_2$-SB-THCA and MNPs@SiO$_2$-SB-THCTA.

Table 3. Kinetic Parameters of Pseudo-First Order and Pseudo-Second Order

samples	pseudo-first order			pseudo-second order		
	q_e (mg g^{-1})	K_1 (min^{-1})	R^2	q_e (mg g^{-1})	K_2 (g mg^{-1} min^{-1})	R^2
MNPs@SiO$_2$-SB-THCA	0.371	2.192×10^{-5}	0.54	14.314	−505.615	0.97
MNPs@SiO$_2$-SB-THCTA	0.288	6.017×10^{-5}	0.56	15.538	−309.144	0.89

THCA and MNPs-SiO$_2$-SB-THCTA, respectively. The removal efficiency of Cr(VI), with a significant decrease at pH 8. The maximum removal efficiency for the two-adsorbent was observed at pH 6, due to the decrease in H$^+$ presence and an increase in available binding sites, resulting in an increased removal efficiency. However, at pH 8, there was a dramatic decrease in removal efficiency due to competition between hydroxyl (OH$^-$) and CrO$_4^{2-}$ "Supporting Information: pH before and after adsorption of Cr(VI)".

3.3. Adsorption Kinetics. Adsorption kinetic models that examine the relationship among concentration, adsorption time, and equilibrium adsorption capacity are critical. The following first-order pseudo (eq 3) can be used to understand the control steps of the adsorption rate of MNPs-SiO$_2$-SB-THCA and MNPs-SiO$_2$-SB-THCTA "Supporting Information: kinetic modeling for adsorption of Cr(VI)"

$$\ln(q_e - q_t) = \ln q_e - K_1 t \tag{3}$$

These relevant experimental data on the adsorption capacity of Cr(VI) ions at different time periods were analyzed using a pseudo-second-order (eq 4). The adsorption capacity of MNPs-SiO$_2$-SB-THCA and MNPs-SiO$_2$-SB-THCTA is given by q_e (mg/g). In adsorption equilibrium, q_t (mg/g) reflects the adsorption capacity of MNPs-SiO$_2$-SB-THCA and MNPs-SiO$_2$-SB-THCTA on Cr(VI) ions at a certain time point, K_1 (h^{-1}) is the first-order pseudorate constant, and K_2 [g/(mg·h)] is the second-order pseudorate constant

$$\frac{t}{q_t} = \frac{1}{K_2 \cdot q_e^2} + \frac{1}{q_e} t \tag{4}$$

The linearity of the kinetics models based on $\ln(q_e - q_t)$ and $\frac{t}{q_t}$

vs time (min).

The kinetic parameters of the adsorption of Cr(VI) ions on the surface of the sorbents MNPs-SiO$_2$-SB-THCA and MNPs-SiO$_2$-SB-THCTA were estimated from the intercepts and slopes. According to the observed results, the pseudo-second order kinetic model for MNPs-SiO$_2$-SB-THCA and MNPs-SiO$_2$-SB-THCTA better describes the experimental data (Table 3).

The calculated adsorption capacity for MNPs@SiO$_2$-SB-THCA is 14.31 and 15.53 mg/g for MNPs@SiO$_2$-SB-THCTA. Furthermore, these results are confirmed by R^2 correlation coefficients of 0.97 and 0.89, which are both close to 1.

3.4. Adsorption Isotherms. In order to understand the adsorption system between adsorbate and adsorbent, an understanding of the adsorption isotherms is required.[42] To better understand the interaction between Cr(VI) ions, MNPs@SiO$_2$-SB-THCA and MNPs@SiO$_2$-SB-THCTA in the adsorption process, Langmuir, Freundlich, and Temkin isotherms were established to evaluate the adsorption data. The formulas are as follows:

The Langmuir adsorption isotherm (eq 5) is as follows

$$\frac{C_e}{q_e} = \frac{C_e}{Q_m} + \frac{1}{Q_m K} \tag{5}$$

Freundlich adsorption isotherm (eq 6)

$$\log q_e = \log K_F + \frac{1}{n} \log C_e \tag{6}$$

Temkin adsorption isotherm (eq 7)

$$q_e = \frac{RT}{b} \ln K_T + \frac{RT}{b} \ln C_e \tag{7}$$

where C_e is the equilibrium concentration of Cr(VI) ions in mg/L, Q_e and Q_m are the adsorption capacity and saturation adsorption capacity in (mg/g), and K (L/mg) is the Langmuir constant. K_F (L/mg) is a constant that could represent the saturated adsorption amount in the Freundlich adsorption isotherm model and $1/n$ is an empirical parameter that reflects the adsorption intensity. The adsorption intensity changes with material heterogeneity in the Freundlich adsorption isotherm model. The Temkin value K_T stands for the equilibrium binding constant (L mol^{-1}), b for the heat of adsorption, and T for the temperature.[43]

The adsorption isotherm model, which applies to both single-layer and multi-layer adsorption, has been used in a large number of studies of the adsorption mechanism. As a result, the adsorption isotherm model is often used to study the

Table 4. Langmuir, Freundlich, and Temkin Isotherms Data for the Adsorption of Cr(VI) Ions on the Surface of MNPs-SiO$_2$-SB-THCA and MNPs-SiO$_2$-SB-THCTA

adsorbents	Langmuir isotherm			Freundlich isotherm			Temkin isotherm		
	Q_{max} (mg/g)	K_L	R^2	K_F	$1/n$	R^2	K_T (L/mg)	b_T (J/mol)	R^2
MNPs-SiO$_2$-SB-THCA	5.376	0.014	0.99	0.0125	1.697	0.99	0.069	6.563	0.89
MNPs-SiO$_2$-SB-THCTA	2.775	0.025	0.76	20.074	2.465	0.69	2.868	13.581	0.76
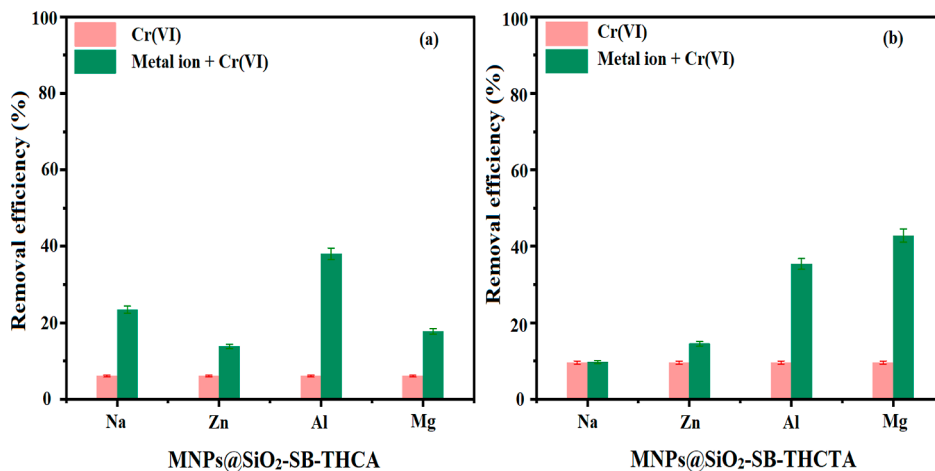
Figure 10. Influence metal cation on (a) MNPs@SiO$_2$-SB-THCA and (b) MNPs@SiO$_2$-SB-THCTA adsorption of Cr(IV), pH 6, adsorbent dose 10 mg, contact duration 180 min, temperature 298 K, ion concentration 5 ppm, and Cr(VI) concentration 50 ppm.

adsorption mechanism throughout the sorption process. The adsorption effect is strongly influenced by the temperature of the adsorption environment.

The displayed diagram of the Freundlich model is closer to the experimental diagrams than the printed diagrams of the Langmuir and Temkin model. Table 4 summarizes the data obtained. MNPs-SiO$_2$-SB-THCA and MNPs-SiO$_2$-SB-THCTA had consistent K_L (0.014 and 0.025 L/mg), K_F (0.0125 and 20.074 L/mg), and K_T (0.069 and 2.868 L/mg). The correlation regressions for the two adsorbents were 0.99 and 0.76 for Langmuir, 0.99 and 0.69 for Freundlich, and 0.89 and 0.76 for Temkin.

The higher values of the Freundlich correlation coefficients indicate that the Freundlich isotherm model describes the adsorption of Cr(VI) ions on the surface of MNPs-SiO$_2$-SB-THCA and MNPs-SiO$_2$-SB-THCTA are better than the isotherm models of Langmuir and Temkin.

3.5. Thermodynamic Studies. Temperature influences the effect of MNPs-SiO$_2$-SB-THCA and MNPs-SiO$_2$-SB-THCTA on the removal of Cr(VI) in wastewater, which is explained by thermodynamic factors "Supporting Information: thermodynamic graph of Cr(VI) adsorption". The changes in Gibbs free energy ($\Delta G°$, kJ/mol), enthalpy ($\Delta H°$, kJ/mol), and entropy ($\Delta S°$, kJ/mol) are evaluated to determine whether the adsorption is spontaneous, endothermic, or exothermic.

The adsorption thermodynamics equations are (eqs 8−10)

$$\Delta G° = -RT \ln(K_c) \tag{8}$$

$$\mathrm{Ln}(K_c) = \frac{\Delta S°}{R} - \frac{\Delta H°}{RT} \tag{9}$$

$$K_c = \frac{Q_e}{C_e} \tag{10}$$

The standard R stands for the molar gas constant (8.314 J K mol^{-1}), the standard T for the temperature (K), and the standard K_c for the thermodynamic constant.

The thermodynamic graphs for the adsorption of Cr(VI) on the surfaces of MNPs-SiO$_2$-SB-THCA and MNPs-SiO$_2$-SB-THCTA are shown in Figure 10. The values of $\Delta H°$ and $\Delta S°$ were estimated from the slope and intercept of the graphs shown, and the data are summarized in Table 4. The parameter $\Delta G°$ was used to investigate the physical adsorption or chemisorption in the process. Adsorption is spontaneous when the $\Delta G°$ value is negative. Positive $\Delta H°$ values indicate that the process is endothermic. A negative $\Delta S°$ value indicates a shift in randomness at the solid/solution interface.[44]

The type of adsorption process is described by the $\Delta H°$ value. In the present study, $\Delta H°$ corresponded to 2.27 and 1.57 kJ/mol, indicating a physicochemical adsorption process rather than a purely physical or chemical adsorption mechanism. The $\Delta S°$ values in this study were −0.609 and −3.67 kJ/mol. Endothermic and random adsorption are indicated by positive $\Delta H°$ and negative $\Delta S°$ values, respectively. $\Delta G°$ values of only −0.18 and −0.39 kJ/mol indicate a physical adsorption process with electrostatic interaction between sorption sites and Cr(VI) ions (Table 5).

3.6. Mechanism of Adsorption Process. The ability of the adsorbent to form complexes is due to the chelating properties of its N and S donor atoms. This leads to a strong and stable complex. In addition, the amide groups in thiophene provide a high electron density over that of the sulfur atom. This improves the binding ability of the adsorbent and enables the formation of a strong bond between Cr(III) and the Schiff base and sulfur in the adsorbent. As mentioned in the last study[45] on the electroactive nature of polythiophene, we cannot ignore the redox reactions of Cr(VI) to Cr(III) ions that could be formed during the redox reaction.

Table 5. Thermodynamic Parameters of Cr(VI) Adsorption on the Surface MNPs-SiO$_2$-SB-THCA and MNPs-SiO$_2$-SB-THCTA

adsorbents	C_0 (mg/L)	T (K)	$\Delta G°$ (kJ/mol)	$\Delta H°$ (kJ/mol)	$\Delta S°$ (kJ·mol^{-1} K^{-1})
MNPs@SiO$_2$-SB-THCA	50	298	−0.53	2.27	−6.09
		308	−0.18		
		318	−0.42		
MNPs@SiO$_2$-SB-THCTA	50	298	−0.50	1.57	−3.67
		308	−0.39		
		318	−0.43		

XPS analysis was used to investigate the adsorption process by using the XPS spectra before and after adsorption. As shown in "Supporting Information: XPS spectra of adsorbed materials before and after adsorption", after the absorption of Cr(VI) in MNPs@SiO$_2$-SB-THCA, the C 1s fit of O=C−NH$_2$, C=C, C−C, C=N, and C−H/C−S shifted from 289.47, 288.48, 287.47, 286.45, and 285.93 to 291.3, 288.5, 287.83, 287.27, and 286.78 eV, respectively. Similar results were also observed for the absorption of Cr(VI) in MNPs@SiO$_2$-SB-THCTA, where the S=C−NH$_2$, C=C, C−C, C=N, and C−H/C−S shifted from 289.43, 287.95, 287.18, 286.53, and 285.81 to 290.34, 288.17, 286.33, 286.38, and 286.11 eV, respectively.

The binding energy in N 1s for C=N also shifted from 401.17 to 399.19 eV after adsorption of Cr(VI) in MNPs@SiO$_2$-SB-THCA and for MNPs@SiO$_2$-SB-THCTA from 400.65 to 401.4 eV after adsorption. Table 6 shows the

Table 6. Binding Energy and Relative Content (%) of C 1s and N 1s for MNPs@SiO$_2$-SB-THCA and MNPs@SiO$_2$-SB-THCTA Before and After Adsorption of Cr(VI) at pH 6

valence state	carbon states	MNPs@SiO$_2$-SB-THCA		MNPs@SiO$_2$-SB-THCTA	
		before adsorption	after adsorption	before adsorption	after adsorption
C 1s	C−S/C−H	11.62	26.98	20.17	17.25
	C−C	17.77	13.12	16.67	12.05
	C=N	12.78	4.74	15.63	1.69
	C=C	8.58	46.69	17.88	17.09
	C=O−NH$_2$/C=S−NH$_2$	49.25	8.7	29.65	51.92

valence state	nitrogen states	MNPs@SiO$_2$-SB-THCA		MNPs@SiO$_2$-SB-THCTA	
		before adsorption	after adsorption	before adsorption	after adsorption
N 1s	C=N	6.56	29.77	29.45	64.03
	C=O−NH$_2$/C=S−NH$_2$	93.44	70.23	70.55	35.97

relative percentage of carbon. The percentage of C=N decreases from 12.78 to 4.74% after adsorption of Cr(VI) in MNPs@SiO$_2$-SB-THCA. For the other adsorbent MNPs@SiO$_2$-SB-THCTA, the percentage also decreases from 15.63% to 1.69%. This shows that C=N plays an important role in the adsorption of Cr(VI).
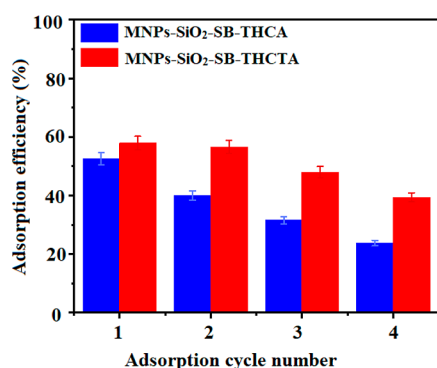
The binding energy of Cr 2p is listed in Table 7. The oxidation state of the MNPs@SiO$_2$-SB-THCA for Cr(III) is 41.2% and Cr(VI) is 58.8%. The other adsorbent MNPs@SiO$_2$-SB-THCTA for Cr(III) was 45%, and Cr(VI) was 55%. This indicates that most of the Cr undergoes hexavalent oxidation and some of it is reduced to Cr(III) by a redox reaction. The redox reaction could occur through the NH$_2$ groups in the amide as electron-donating groups. The XPS of the N 1s spectra for O=C−NH$_2$ and S=C−NH$_2$ show a shift of the binding energy from 402.94 to 402.81 eV in MNPs@SiO$_2$-SB-THCA after adsorption. For MNPs@SiO$_2$-SB-THCTA, the energy shifted from 401.84 to 402.81.

3.7. Competitive Adsorption. The competitive removal efficiency of MNPs@SiO$_2$-SB-THCA (Figure 10a) and MNPs@SiO$_2$-SB-THCTA (Figure 10b) was investigated in the presence of additional anions Na$^+$, Zn^{2+}, Al^{3+}, and Mg^{2+}. The results showed that metal cations enhanced the adsorption of Cr(VI). In particular, Na$^+$, Zn^{2+}, Al^{3+}, and Mg^{2+} all showed positive effects on the Cr(VI) removal efficiency of MNPs@SiO$_2$-SB-THCA (increased by 17.3, 7.7, 31.9, and 11.6%). The second materials MNPs@SiO$_2$-SB-THCA increased by 0.1, 4.9, 25.7, and 33.1%, respectively. This could be due to the fact that metal cations on the surface were absorbed by both MNPs@SiO$_2$-SB-THCA and MNPs@SiO$_2$-SB-THCTA, which increased the electrostatic attraction with HCrO$_4^-$ and CrO$_4^{2-}$.[46−48]

3.8. Regeneration Analysis. For the regeneration analysis, 45 mg of adsorbent was mixed with 30 mL of a 50 ppm of Cr(VI) solution at 25 °C. After the adsorption procedure, the adsorbent was extracted by centrifugation and magnetic separation. The adsorbent was then recycled 3 times with 0.5 mol/L NaOH for 30 mL, 3 times for 10 min, and 3 times with 30 mL of water. The adsorbent was then dried at 60 °C for 6 h before being used for four adsorption cycles. The clearance rate of MNPs@SiO$_2$-SB-THCTA was 57.87 and 56.56% in the first two cycles, as shown in Figure 11. The decrease in adsorption effectiveness could be due to the loss of certain nanoparticles during the washing step to recycle the adsorbent.

Table 8 shows a comparison between the synthesized MNPs-SiO$_2$-SB-THCA and MNPs-SiO$_2$-SB-THCTA and the previously published[47−53] sorbents used to remove Cr(VI) ions from contaminated water. The results of the current study under optimal conditions (0.01 g/L adsorbent dose, 298 K temperature, 1 h contact time, and pH 6) confirmed that the proposed sorbents with a low dose of 0.01 g/L provide efficient removal of Cr(VI) ions with removal capacities of 15.5

Table 7. Cr 2p Peak for MNPs@SiO$_2$-SB-THCA and MNPs@SiO$_2$-SB-THCTA Before and After Adsorption of Cr(VI) at pH 6

valence state	species	parameters	MNPs@SiO$_2$-SB-THCA		MNPs@SiO$_2$-SB-THCTA	
			2p$_{3/2}$	2p$_{1/2}$	2p$_{3/2}$	2p$_{1/2}$
Cr 2p	Cr(III)	peak position	583.05	590.07	575.94	583.63
		content (%)	29.02	12.18	25.95	19.05
	Cr(VI)	peak position	580.16	587.37	579.80	588.3
		content (%)	44.50	14.30	31.35	23.65

Figure 11. Recyclability of the synthesized MNPs-SiO₂-SB-THCA and MNPs-SiO₂-SB-THCTA.

and 14.3 mg/g, respectively. The experimental conditions in the present work are consistent with the other reported methods[51−53] in terms of initial Cr(VI) concentration, contact time, and temperature. The advantage of the current method is that the removal efficiency can be performed in a wide pH range of 2−8. Therefore, the synthesized MNPs-SiO₂-SB-THCA and MNPs-SiO₂-SB-THCTA can be used as ideal adsorbents for the removal of Cr(IV) from groundwater effluents, even if the water is alkaline.[54]

4. CONCLUSIONS

This study describes the preparation of an organic ligand by using the Vilsmeier−Haack reaction. The formed aldehyde groups in thiophene derivatives were used to link the organic compound to the surface of modified iron oxide nanoparticles through amine groups to form a C=N bond. The grafting process was carried out using two main techniques, one homogeneous and one heterogeneous. The synthesized materials were characterized by FT-IR, XRD, NMR, TEM, TGA, and XPS. The XPS and TGA results confirmed that the homogeneous technique exhibited excellent grafting compared to the heterogeneous technique. Both the modified MNPs@SiO₂-SB-THCA and the MNPs@SiO₂-SB-THCTA compounds were prepared using the homogeneous technique. The effect of pH in the range of 2−8 on the adsorption capacity of Cr(VI) was investigated using the previously prepared modified materials and the critical parameters such as contact time, adsorption dose, and initial concentration. The adsorption kinetics were investigated, and it was found that the

removal process obeys a pseudo-second reaction. The adsorption isotherm was fitted by using the Freundlich model. It was found that the two adsorbents have a high adsorption capacity at pH 6. The adsorption capacities were 14.31 and 15.53 mg/g for MNPs@SiO₂-SB-THCTA, respectively.

■ ASSOCIATED CONTENT

Data Availability Statement
All data have been included within the text.

ⓢ Supporting Information
The Supporting Information is available free of charge at https://pubs.acs.org/doi/10.1021/acsomega.3c07517.

> pH before and after adsorption of Cr(VI) into MNPs@SiO₂-SB-THCA and MNPs@SiO₂-SB-THCTA; kinetic modeling with pseudo-first order and pseudo-second order; thermodynamic graph of Cr(VI) adsorption; and XPS spectra of the adsorbent before and after adsorption of Cr(VI) (PDF)

■ AUTHOR INFORMATION

Corresponding Author
Seham S. Alterary − *Department of Chemistry, College of Science, King Saud University, 11495 Riyadh, Saudi Arabia;* ⓞ orcid.org/0000-0002-4176-2840; Email: salterary@ksu.edu.sa

Authors
Monirah A. Al-Alshaikh − *Department of Chemistry, College of Science, King Saud University, 11495 Riyadh, Saudi Arabia*
Athar M. Elhadi − *Department of Chemistry, College of Science, King Saud University, 11495 Riyadh, Saudi Arabia*
Wenjie Cao − *Scientific Design Company Incorporated, Little Ferry 07643 New Jersey, United States*

Complete contact information is available at:
https://pubs.acs.org/10.1021/acsomega.3c07517

Author Contributions
Conceptualization and funding acquisition, S.S.A.; supervision and writing-original draft preparation, M.A.A.-A. Methodology, formal analysis, investigation, and data curation, A.M.E. All authors have read and agreed to the published version of the manuscript.

Table 8. Comparison between the Synthesized MNPs-SiO₂-SB-THCA and MNPs-SiO₂-SB-THCTA and the Previously Published Sorbents for the Removal of Cr(VI) Ions

adsorbents	adsorption conditions					isotherm model	Q_{max} (mg/g)	refs
	initial C_0 (mg/L)	pH	temp. (K)	contact time (h)	sorbent dosage			
biochar and activated carbon	100	2	298	12	2.0 g/L	Langmuir	45.3	49
nitrogen-doped carboxylated porous carbon	200	3	298	1.5	1.0 g/L	Langmuir	104	50
3-MPA-coated SPION	10	1	298	1	0.5 g/mL	Langmuir, Freundlich	45	51
APTES@TEOS@MNP	100	2.5	298	1	0.02 g/L	Langmuir	35	52
nitrogen doping hydrothermal carbon material	50	2	298	1	1.0 g/L	Langmuir	99	53
MNPs@SiO₂-SB-THCTA	50	6	298	1	0.01 g/L	Freundlich	15.5	current study
MNPs@SiO₂-SB-THCA	50	6	298	1	0.01 g/L	Freundlich	14.3	

Notes

The authors declare no competing financial interest.

■ REFERENCES

(1) Ethaib, S.; Zubaidi, S. L. Removal of methylene blue dye from aqueous solution using kaolin. In *IOP Conference Series: Materials Science and Engineering, Proceedings of the 2nd International Scientific Conference of Al-Ayen University, Nasiriyah, Iraq,* 15−16 July; IOP Publishing: Bristol, UK, 2020.

(2) Burakov, A. E.; Galunin, E. V.; Burakova, I. V.; Kucherova, A. E.; Agarwal, S.; Tkachev, A. G.; Gupta, V. K. Adsorption of heavy metals on conventional and nanostructured materials for wastewater treatment purposes: a review. *Ecotoxicol. Environ. Saf.* 2018, 148, 702−712.

(3) Pakade, V. E.; Tavengwa, N. T.; Madikizela, L. M. Recent advances in hexavalent chromium removal from aqueous solutions by adsorptive methods. *RSC Adv.* 2019, 9, 26142−26164.

(4) Zulfiqar, U.; Haider, F. U.; Ahmad, M.; Hussain, S.; Maqsood, M. F.; Ishfaq, M.; Shahzad, B.; Waqas, M. M.; Ali, B.; Tayyab, M. N.; Ahmad, S. A.; et al. Chromium toxicity, speciation, and remediation strategies in soil-plant interface: A critical review. *Front. Plant Sci.* 2023, 13, 1081624.

(5) Saleem, H.; Zaidi, S. J. Developments in the application of nanomaterials for water treatment and their impact on the environment. *Nanomaterials* 2020, 10, 1764.

(6) Goswami, M. K.; Srivastava, A.; Dohare, R. K.; Tiwari, A. K.; Srivastav, A. Recent advances in conducting polymer-based magnetic nano sorbents for dyes and heavy metal removal: fabrication, applications, and perspective. *Environ. Sci. Pollut. Res.* 2023, 30, 73031−73060.

(7) Meng, X.; Li, J.; Lin, Y.; Liu, X.; Li, D.; He, Z. Nanotechnology for purifying nematic liquid crystals based on magnetic separation accompanied by phase transition. *J. Colloid Interface Sci.* 2023, 640, 61−66.

(8) Khare, P.; Bhati, A.; Anand, S. R.; Gunture; Sonkar, S. K. Brightly Fluorescent Zinc-Doped Red-Emitting Carbon Dots for the Sunlight-Induced Photoreduction of Cr(VI) to Cr(III). *ACS Omega* 2018, 3, 5187−5194.

(9) Saini, D.; Kaushik, J.; Garg, A. K.; Dalal, C.; Sonkar, S. K. N, S-co-doped carbon dots for nontoxic cell imaging and as a sunlight-active photocatalytic material for the removal of chromium. *ACS Appl. Bio Mater.* 2020, 3, 3656−3663.

(10) Kumari, P.; Tripathi, K. M.; Awasthi, K.; Gupta, R. Sustainable carbon nano-onions as an adsorbent for the efficient removal of oxo-anions. *Environ. Sci. Pollut. Res.* 2022, 30, 15480−15489.

(11) Nyairo, W. N.; Shikuku, V. O.; Sanou, Y. Carbon nanotubes in water treatment: Progress and challenges. In *Innovative Nano-composites for the Remediation and Decontamination of Wastewater*; IGI Global, 2022; pp 171−184.

(12) Bhaduri, B.; Dikshit, A. K.; Kim, T.; Tripathi, K. M. Research Progress and Prospects of Spinel Ferrite Nanostructures for the Removal of Nitroaromatics from Wastewater. *ACS Appl. Nano Mater.* 2022, 5, 16000−16026.

(13) Lu, W.; Li, J.; Sheng, Y.; Zhang, X.; You, J.; Chen, L. One-pot synthesis of magnetic iron oxide nanoparticle-multiwalled carbon nanotube composites for enhanced removal of Cr (VI) from aqueous solution. *J. Colloid Interface Sci.* 2017, 505, 1134−1146.

(14) Enache, D. F.; Vasile, E.; Simonescu, C. M.; Razvan, A.; Nicolescu, A.; Nechifor, A. C.; Oprea, O.; Pătescu, R. E.; Onose, C.; Dumitru, F. Cysteine-functionalized silica-coated magnetite nano-particles as potential nanoadsorbents. *J. Solid State Chem.* 2017, 253, 318−328.

(15) Tlili, H.; Elaoud, A.; Asses, N.; Horchani-Naifer, K.; Ferhi, M.; Goya, G. F.; Fuentes-Garcia, J. A. Reduction of oxidizable pollutants in waste water from the Wadi El Bey river basin using magnetic nanoparticles as removal agents. *Magnetochemistry* 2023, 9, 157.

(16) Ethaib, S.; Al-Qutaifia, S.; Al-Ansari, N.; Zubaidi, S. L. Function of Nanomaterials in Removing Heavy Metals for Water and Wastewater Remediation: A Review. *Environments* 2022, 9, 123.

(17) Qasem, N. A. A.; Mohammed, R. H.; Lawal, D. U. Removal of heavy metal ions from wastewater: a comprehensive and critical review. *npj Clean Water* 2021, 4, 36.

(18) Behbahani, E. S.; Dashtian, K.; Ghaedi, M. Fe₃O₄-FeMoS₄: Promise magnetite LDH-based adsorbent for simultaneous removal of Pb (II), Cd (II), and Cu (II) heavy metal ions. *J. Hazard Mater.* 2021, 410, 124560.

(19) Wang, J.; Han, Q.; Wang, K.; Li, S.; Luo, W.; Liang, Q.; Zhong, J.; Ding, M. Recent advances in development of functional magnetic adsorbents for selective separation of proteins/peptides. *Talanta* 2023, 253, 123919.

(20) Lu, W.; Li, J.; Sheng, Y.; Zhang, X.; You, J.; Chen, L. One-pot synthesis of magnetic iron oxide nanoparticle-multiwalled carbon nanotube composites for enhanced removal of Cr (VI) from aqueous solution. *J. Colloid Interface Sci.* 2017, 505, 1134−1146.

(21) Jawad, A. A.; Mahmoud, Z. H.; Kadhim, M. M.; Rheima, A. M.; Abbas, Z. S.; Al-bayati, A. D. J.; Abed, Z. T.; Al-Jaafari, F. M. D.; Jaber, A. S.; Hachim, S. K.; et al. Functionalize and supercapacitor performance of magnetic oxide nanoparticles. *Inorg. Chem. Commun.* 2023, 154, 110884.

(22) Tian, R.; Gao, Z.; Chen, G.; Guan, H.; Dong, C.; Comini, E. Functionalized Pt nanoparticles between α/γ-Fe₂O₃ and MXene for superior acetone sensing. *Sens. Actuators, B* 2023, 383, 133584.

(23) Shigemoto, A. K.; Killjoy, A. A.; Dayton, J.; Virca, C. N.; McCormick, T. M. Increased binding of thiophene-based ligands to mercury (ii) with water solubilizing functional groups. *Mol. Syst. Des. Eng.* 2020, 5, 1024−1036.

(24) Kumagai, T.; Kinoshita, B.; Hirashima, S.; Sugiyama, H.; Park, S. Thiophene-Extended Fluorescent Nucleosides as Molecular Rotor-Type Fluorogenic Sensors for Biomolecular Interactions. *ACS Sens.* 2023, 8, 923−932.

(25) Malik, M. A.; Dar, O. A.; Gull, P.; Wani, M. Y.; Hashmi, A. A. Heterocyclic Schiff base transition metal complexes in antimicrobial and anticancer chemotherapy. *MedChemComm* 2018, 9, 409−436.

(26) Zhang, Y.; Cao, X.; Sun, J.; Wu, G.; Wang, J.; Zhang, D. Synthesis of pyridyl Schiff base functionalized sba-15 mesoporous silica for the removal of cu (ii) and pb (ii) from aqueous solution. *J. Sol-Gel Sci. Technol.* 2020, 94, 658−670.

(27) Suleymanoglu, N.; Demir, E. E.; Direkel, S.; Unver, Y. Theoretical study and antimicrobial activities of new Schiff-base derivatives with thiophene. *J. Mol. Struct.* 2020, 1218, 128522.

(28) Wang, Y.; Tang, M.; Shen, H.; Che, G.; Qiao, Y.; Liu, B.; Wang, L. Recyclable Multifunctional Magnetic Mesoporous Silica Nano-composite for Ratiometric Detection, Rapid Adsorption, and Efficient Removal of Hg(II). *Chem. Eng.* 2018, 6, 1744−1752.

(29) Zhao, Z.; Sun, S.; Wu, D.; Zhang, M.; Huang, C.; Umemura, K.; Yong, Q. Synthesis and characterization of sucrose and ammonium dihydrogen phosphate (SADP) adhesive for plywood. *Polymers* 2019, 11, 1909.

(30) Culita, D. C.; Simonescu, C. M.; Patescu, R. E.; Dragne, M.; Stanica, N.; Oprea, O. o-Vanillin functionalized mesoporous silica-coated magnetite nanoparticles for efficient removal of Pb (II) from water. *J. Solid State Chem.* 2016, 238, 311−320.

(31) Liu, Z.; Lei, M.; Zeng, W.; Li, Y.; Li, B.; Liu, D.; Liu, C. Synthesis of magnetic Fe₃O₄@ SiO₂(-NH₂/-COOH) nanoparticles and their application for the removal of heavy metals from wastewater. *Ceram. Int.* 2023, 49, 20470−20479.

(32) Zhao, J.; Niu, Y.; Ren, B.; Chen, H.; Zhang, S.; Jin, J.; Zhang, Y. Synthesis of Schiff base functionalized superparamagnetic Fe₃O₄ composites for effective removal of Pb (II) and Cd (II) from aqueous solution. *Chem. Eng. J.* 2018, 347, 574−584.

(33) Sun, J.; Xu, Z.; Li, W.; Shen, X. Effect of nano-SiO_2 on the early hydration of alite-sulphoaluminate cement. *Nanomaterials* **2017**, *7*, 102.

(34) Bratskaya, S. Y.; Ustinov, A. Y.; Azarova, Y. A.; Pestov, A. V. Thiocarbamoyl chitosan: synthesis, characterization and sorption of Au (III), Pt (IV), and Pd (II). *Carbohydr. Polym.* **2011**, *85*, 854−861.

(35) Wang, Y.; Tang, M.; Shen, H.; Che, G.; Qiao, Y.; Liu, B.; Wang, L. Recyclable Multifunctional Magnetic Mesoporous Silica Nanocomposite for Ratiometric Detection, Rapid Adsorption, and Efficient Removal of Hg(II). *Chem. Eng.* **2018**, *6*, 1744−1752.

(36) Sun, J.; Xu, Z.; Li, W.; Shen, X. Effect of nano-SiO_2 on the early hydration of alite-sulphoaluminate cement. *Nanomaterials* **2017**, *7*, 102.

(37) Gorobets, N. Y.; Yermolayev, S. A.; Gurley, T.; Gurinov, A. A.; Tolstoy, P. M.; Shenderovich, I. G.; Leadbeater, N. E. Difference between ^{1}H NMR signals of primary amide protons as a simple spectral index of the amide intramolecular hydrogen bond strength. *J. Phys. Org. Chem.* **2012**, *25*, 287−295.

(38) Akram, M.; Bhatti, H. N.; Iqbal, M.; Noreen, S.; Sadaf, S. Biocomposite efficiency for Cr (VI) adsorption: Kinetic, equilibrium and thermodynamics studies. *J. Environ. Chem. Eng.* **2017**, *5*, 400−411.

(39) Batool, F.; Akbar, J.; Iqbal, S.; Noreen, S.; Bukhari, S. N. A. Study of isothermal, kinetic, and thermodynamic parameters for adsorption of cadmium: an overview of linear and nonlinear approach and error analysis. *Bioinorg. Chem. Appl.* **2018**, *2018*, 1−11.

(40) Mondal, N. K.; Samanta, A.; Chakraborty, S.; Shaikh, W. A. Enhanced chromium (VI) removal using banana peel dust: isotherms, kinetics and thermodynamics study. *Sustain. Water Resour. Manag.* **2018**, *4*, 489−497.

(41) Gupta, A. K.; Kumar, A.; Maurya, U. K.; Singh, D.; Islam, S.; Rathore, A. C.; Kumar, P.; Singh, R.; Madhu, M. Comprehensive spatio-temporal benchmarking of surface water quality of Hindon River, a tributary of river Yamuna, India: Adopting multivariate statistical approach. *Environ. Sci. Pollut. Res.* **2022**, *30*, 116804−116830.

(42) Li, Z.; Sellaoui, L.; Luiz Dotto, G.; Bonilla-Petriciolet, A.; Ben Lamine, A. Understanding the adsorption mechanism of phenol and 2-nitrophenol on a biopolymer-based biochar in single and binary systems via advanced modeling analysis. *Chem. Eng. J.* **2019**, *371*, 1−6.

(43) Debnath, S.; Das, R. Strong adsorption of CV dye by Ni ferrite nanoparticles for waste water purification: Fits well the pseudo second order kinetic and Freundlich isotherm model. *Ceram. Int.* **2023**, *49*, 16199−16215.

(44) Elkony, A. M.; Ibrahim, A. G.; Abu El-Farh, M. H.; Abdelhai, F. Synthesis of Acrylamide-co-3-Allyloxy-2-hydroxy-1-propanesulfonic acid sodium salt Hydrogel for efficient Adsorption of Methylene blue dye. *Int. J. Environ. Anal. Chem.* **2023**, *103*, 1751−1770.

(45) Duan, G.; Li, X.; Ma, X.; Zhong, W.; Wang, S. High-efficiency adsorption removal for Cu (II) and Ni (II) using a novel acylamino dihydroxamic acid chelating resin. *Sci. Total Environ.* **2023**, *864*, 160984.

(46) Kaur, M.; Kumar, S.; Yusuf, M.; Lee, J.; Malik, A. K.; Ahmadi, Y.; Kim, K. H. Schiff base-functionalized metal-organic frameworks as an efficient adsorbent for the decontamination of heavy metal ions in water. *Environ. Res.* **2023**, *236*, 116811.

(47) Cheng, H.; Liu, Y.; Li, X.; He, H.; Kang, X. Efficient recovery of Cr(vi) from electroplating wastewater by iron-modified sludge-based hollow-structured porous carbon: coexistence effects and competition for adsorption. *RSC Adv.* **2021**, *11*, 37233−37245.

(48) Du, L.; Gao, P.; Meng, Y.; Liu, Y.; Le, S.; Yu, C. Highly efficient removal of Cr (VI) from aqueous solutions by polypyrrole/monodisperse latex spheres. *ACS Omega* **2020**, *5*, 6651−6660.

(49) Wu, Z.; Zhang, H.; Ali, E.; Shahab, A.; Huang, H.; Ullah, H.; Zeng, H. Synthesis of novel magnetic activated carbon for effective Cr (VI) removal via synergistic adsorption and chemical reduction. *Environ. Technol. Innovat.* **2023**, *30*, 103092.

(50) Bakry, A. M.; Awad, F. S.; Bobb, J. A.; El-Shall, M. S. Multifunctional binding sites on nitrogen-doped carboxylated porous carbon for highly efficient adsorption of Pb (II), Hg (II), and Cr (VI) ions. *ACS Omega* **2020**, *5* (51), 33090−33100.

(51) Burks, T.; Avila, M.; Akhtar, F.; Göthelid, M.; Lansåker, P. C.; Toprak, M. S.; Muhammed, M.; Uheida, A. Studies on the adsorption of chromium (VI) onto 3-Mercaptopropionic acid coated superparamagnetic iron oxide nanoparticles. *J. Colloid Interface Sci.* **2014**, *425*, 36−43.

(52) Gallo-Cordova, A.; Morales, M. D. P.; Mazarío, E. Effect of the surface charge on the adsorption capacity of chromium (VI) of iron oxide magnetic nanoparticles prepared by microwave-assisted synthesis. *Water* **2019**, *11* (11), 2372.

(53) Wei, Y.; Wang, H.; Zhang, X.; Liu, C. Ammonia-assisted hydrothermal carbon material with schiff base structures synthesized from factory waste hemicelluloses for Cr (VI) adsorption. *J. Environ. Chem. Eng.* **2021**, *9* (5), 106187.

(54) Zeng, Q.; Huang, Y.; Huang, L.; Hu, L.; Xiong, D.; Zhong, H.; He, Z. Efficient removal of hexavalent chromium in a wide pH range by composite of SiO_2 supported nano ferrous oxalate. *Chem. Eng. J.* **2020**, *383*, 123209.